JGR Oceans

RESEARCH ARTICLE
10.1029/2020JC016274

Key Points:

- A shipboard broadband acoustic survey was performed at the site of a seafloor-sourced oil spill to determine the flow rate of hydrocarbons
- The rise rate and amplitude and shape of broadband backscatter determined the size, number, and identity (oil or gas) of targets
- The flow rate of liquid hydrocarbons was estimated to be between 56 and 86 barrels per day

Supporting Information:

- Supporting Information S1

Correspondence to:
S. Loranger,
SLoranger@whoi.edu

Citation:
Loranger, S., & Weber, T. C. (2020). Shipboard acoustic observations of flow rate from a seafloor-sourced oil spill. *Journal of Geophysical Research: Oceans*, *125*, e2020JC016274. https://doi.org/10.1029/2020JC016274

Received 26 MAR 2020
Accepted 20 SEP 2020
Accepted article online 15 OCT 2020

Shipboard Acoustic Observations of Flow Rate From a Seafloor-Sourced Oil Spill

Scott Loranger[1,2] **and Thomas C. Weber**[3]

[1]Department of Earth Sciences, University of New Hampshire, Durham, NH, USA, [2]Applied Ocean Physics and Engineering, Woods Hole Oceanographic Institution, Woods Hole, MA, USA, [3]Department of Mechanical Engineering, University of New Hampshire, Durham, NH, USA

Abstract In 2004 a debris flow generated by Hurricane Ivan toppled an oil production platform in Mississippi Canyon lease block 20 (MC20). Between 2004 and the installation of a containment system in 2019 MC20 became an in situ laboratory for a wide range of hydrocarbon in the sea-related research, including different methods of assessing the volumetric flow rate of hydrocarbons spanning different temporal scales. In 2017 a shipboard acoustic Doppler current profiler (ADCP) and high-frequency (90 to 154 kHz) broadband echosounder were deployed to assess the flow rate of liquid and gas phase hydrocarbons. Measurements of horizontal currents were combined with acoustic mapping to determine the rise velocity of the seep as it moved downstream. Models of the rise velocity for fluid particles were used to predict the size of oil droplets and gas bubbles in the seep. The amplitude and shape of the broadband acoustic backscatter were then used to differentiate between, and determine the flow rate of, hydrocarbons. Oil flow rate in the seep was estimated to be 56 to 86 barrels/day (mean = 71 barrels/day) while the flow rate of gaseous hydrocarbons was estimated to be 98 to 359 m^3/day (mean = 229 m^3/day).

Plain Language Summary The Mississippi Canyon block 20 (MC20) oil spill was the result of the toppling of an oil production platform during Hurricane Ivan in 2004. Oil was released from the seafloor where it rose to the surface for 15 years, until a containment system was installed over the leak in 2019. The spill area became a natural laboratory for studying oil released from the seafloor. A variety of measurements over different lengths of time were used to estimate the oil flow rate at MC20 including satellites, shipboard sonars, and sensors on underwater vehicles. We present results from a shipboard sonar method which measured a flow rate of 56 to 86 barrels per day. The value and range of the flow rate varied between the methods used at MC20. This difference could be due to differences among the length of time of measurements, for example, the shipboard sonar measurements were made over 4.5 hr while the containment system measure for about 30 days, or the difference could be due to differences in how the measurements are made. More research is needed to determine how the flow rate of oil rising from the seafloor varies over time to understand how flow rate measurements should be interpreted.

1. Introduction

A variety of methods have been used to determine the flow rate of hydrocarbons from seafloor sources. These methods vary in their limitations and the time scales over which measurements are made. One of the most direct methods of determining the flow rate is the installation of a direct capture containment system (Camilli et al., 2012; Mason et al., 2019). Such systems require vast expenditures in resources for installation and maintenance. Direct capture methods often return a single flow rate estimate integrated over time scales of up to a month. Satellite and surface observations of oil slicks at the sea surface have been used to estimate the flow rate of oil from seafloor sources (Boles et al., 2001; Fingas & Brown, 2018; Hu et al., 2018; MacDonald et al., 2015); however, such measurements only examine the oil and/or gas that has reached the surface and cannot directly determine the flow rate in the water column. Satellite and surface observations often span very long time scales, on the order of years and often include very large ranges of flow rate estimates (see Sun et al., 2018). The estimated flow rate range is more narrow for submersible deployed methods (Camilli et al., 2012; Mason et al., 2019); however, such methods typically use short-range sampling methods and are only capable of sampling a small area at a time. Submersible methods typically cover shorter time scales than satellite and surface observations, on the order of hours to days when

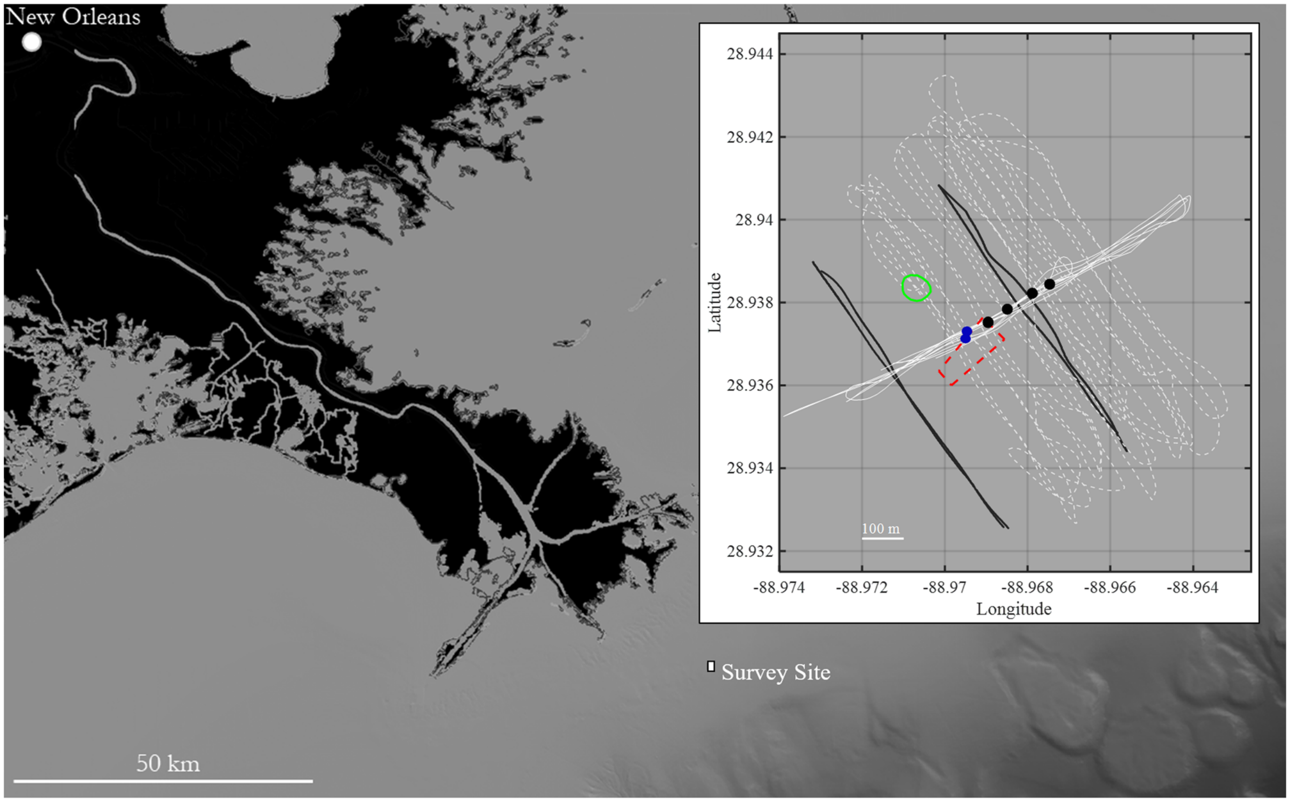

Figure 1. An overview of the survey site in relation to New Orleans with the survey track lines inset. The black-lined white box in the overview shows the area of the inset. In the inset, the black lines are the ADCP survey lines, the dashed white lines are the "across-seep" echosounder surveys, and the solid white lines are the "along-seep" echosounder surveys. The dashed red line shows the location of the downed jacket and the green circle shows the location of the original well bay where the jacket was mounted to the seafloor prior to Hurricane Ivan. The well bay and jacket positions are from Mason et al. (2019). The blue overlapping dots show the source locations as determined in this study and the black dots show the locations of the echograms in Figure 4c–4f. Echograms c–f increase alphabetically with increasing distance from the downed platform.

multiple dives are performed. Shipboard acoustic methods have been used to determine the flow rate of liquid hydrocarbons from anthropogenic seeps (Mason et al., 2019; Weber et al., 2012) and to determine the flow rate of methane from natural seeps (e.g., Hornafius et al., 1999; Padilla et al., 2019; Weber et al., 2014; Wiggins et al., 2015). Shipboard acoustic surveys are capable of making synoptic measures of the entire water column on time scales similar to that of submersible methods. In this study a shipboard broadband acoustic survey was performed to determine the flow rate of hydrocarbons from Mississippi Canyon lease block 20 (MC20).

MC20 is the site of a seafloor-mounted oil production platform that was toppled during Hurricane Ivan in 2004 (Figure 1). A seafloor debris flow generated by the hurricane cut the platform jacket from the well bay and resulted in damage to 25 of the 28 connected wells (Staves et al., 2013). The sea surface in the vicinity of the platform showed a persistent oil slick subsequent to the downing of the jacket (Daneshgar Asl et al., 2016). The seep that persisted over the site for 15 years became an in situ laboratory for a wide range of chemical, biological, and physical oceanography research (see Daneshgar Asl et al., 2016; Harrison, 2017; Herbst et al., 2016; Mason et al., 2019; Staves et al., 2013; Sun et al., 2018; Warren et al., 2014). In 2019 a direct capture containment system was installed at the site to prevent oil from entering the water column (Mason et al., 2019). The installation of the containment system in 2019 provides for a unique opportunity to assess the flow rate of hydrocarbons from a seafloor source and compare it to the relative "known" flow rate measured by the containment system. Satellite (Sun et al., 2018), ROV-based visual (Mason et al., 2019), hybrid shipboard and ROV acoustic (Mason et al., 2019), and direct capture methods have all been used to assess the flow rate at MC20 Table 1. These methods have resulted in a variety of flow rate estimates made over varying time scales and at different times. In this study, the flow rate of hydrocarbons was determined

Table 1
Flow Rate Estimates and Time Scales Over Which Estimates Were Made for the Various Methods Used at MC20

Method	Flow rate (barrels/day)	Time scale of measurement	Survey date	Reference
Satellite	48–1,700	14 years	2005–2016	Sun et al. (2018)
Containment system	24–31	30 days	2019	Mason et al. (2019)
ROV visual	19–108	2 days	2018	Mason et al. (2019)
Broadband shipboard	56–86	4.5 hr	2017	This study
Shipboard acoustic/ROV	9–47	2 hr	2018	Mason et al. (2019)

using a shipboard broadband echosounder in conjunction with current measurements made by a shipboard ADCP. Flow rate estimates other than those discussed here have been conducted at MC20, but only studies that are available in the peer-reviewed literature or have been otherwise archived are reported in Table 1.

One of most significant impediments to acoustically determining flow rate of oil from seafloor sources is the fact that gas bubbles and oil droplets are often collocated. At a single frequency there is an ambiguity between the number and identity of targets; the measured amplitude could be due to a few strong scattering gas bubbles or to many weakly scattering oil droplets. Broadband acoustics have potential to overcome this ambiguity by using the shape and amplitude of the backscatter over a range of frequencies to differentiate between oil and gas. The shape and amplitude of broadband acoustic backscatter has previously been used to differentiate between and identify different targets in the water column (Holliday, 1972; Lavery et al., 2010; Loranger et al., 2019; Medwin & Breitz, 1989; Stanton et al., 2010; Terrill & Melville, 2000; Thompson & Love, 1996; Vagle & Farmer, 1992). Broadband acoustic echosounders also improve range resolution (Weidner et al., 2019) over narrowband systems which helps to separate oil and gas into difference-ensonified volumes. Another benefit of broadband acoustics is the ability to matched filter process the recorded signal. Matched filtering with a broadband signal improves signal-to-noise ratio (Stanton & Chu, 2008; Stanton et al., 2010; Turin, 1960) compared to a narrowband system. The broadband acoustic survey methodology in this study used acoustic mapping of the hydrocarbons present in the water column (referred to as a "seep" in this study) along with measurements of the horizontal currents by ADCP to determine the size of oil and gas in the seep. The amplitude and shape of the backscatter were then used to determine the quantity and identity of targets in each ensonified volume. The volume of oil and gas in each ensonified volume was then integrated to determine the total flow rate of oil and gas in the water column.

2. Acoustic Survey Method

Three sets of acoustic surveys were performed in order to determine the flow rate of oil and gas from this seafloor source: ADCP surveys upstream and downstream of the source, "across-seep" echosounder surveys and "along-seep" echosounder surveys (Table 2, Figure 1). The along-seep passes provided evidence of the presence of two separate sources of hydrocarbons originating from 28.93728°N × − 88.96948°W ± 10 m and 28.93714°N × − 88.96950°W ± 10 m (see supporting information). The sources are arising from the immediate vicinity of the downed jacket (Mason et al., 2019). The position of the sources was determined at 110 m depth, about 25 m above the seafloor and immediately above the downed jacket. The very strong backscatter from the downed jacket masks any signal from the seep at greater depths, and determination of the origin was limited to depths above the jacket. The presence of two sources was in agreement with previous studies of this site (Mason et al., 2019). Note then when distances are given as distance from the seep origin, this refers to the distance from the northern origin.

2.1. ADCP

Horizontal current profiles were measured by a 300 kHz Teledyne-RDI Sentinal V Workhorse acoustic Doppler current profiler (ADCP). The ADCP was pole mounted on the portside of the Gerry Bordelon and

Table 2
Survey Times (UTC) for Surveys Run on 23 September 2017

First ADCP	Across-seep echosounder	Along-seep echosounder	Second ADCP
01:20–01:36	02:27–06:52	07:04–08:38	08:48–09:21

deployed at a depth of about 1.5 m. Raw broadband data were recorded in 6-m-depth bins. Vessel location was determined by a WAAS-enabled GPS. Each ADCP survey consisted of four ~800-m-long lines run perpendicular to the nominal current direction during the time of the experiment (~60°; Figure 1). A preliminary ADCP survey determined the nominal current direction and informed survey locations. Four total lines were run for each ADCP survey; two lines downstream to the southwest of the downed jacket and two lines upstream to the northeast of the jacket. At each location, one line was run heading northwest and then another line was repeated over the same area heading southeast. The sets of lines at each location were run at a speed over ground of about 4 knots. Surveys were run prior to and then again following the echosounder surveys. The times of surveys are listed in Table 2. Details on the ADCP processing methodology can be found in the supporting information.

2.2. Broadband Echosounder

A Kongsberg ES120 echosounder was deployed on the same pole mount as the ADCP on the portside of the R/V Gerry Bordelon. The ES120 (center frequency 120 kHz) was connected to a Kongsberg Wide Band Transceiver (WBT) to enable broadband transmission and reception. A 4 ms linear frequency modulated pulse was transmitted with bandwidth 90–154 kHz. The WBT applies a Tukey window to the transmit signal, resulting in tapered regions within the transmitted frequencies. Data analysis was restricted to frequencies outside the tapered region: 94–153.5 kHz. The ES120 was calibrated in a 12 m × 18 m × 6 m (length × width × depth) fresh water tank at the University of New Hampshire according to the standard sphere method described by Demer et al. (2015).

One kilometer long across-seep survey lines were run perpendicular to the nominal current direction with 50-m line spacing (Figure 1). Successive across-seep lines were run moving upstream from southwest to northeast and then repeated coming back downstream from northeast to southwest. The across-seep lines were used to estimate the position of the hydrocarbon seep in the survey area by visually assessing the recorded echograms in real time and estimating the location of the seep in each across-seep line. Along-seep survey lines were then run over the positions estimated by the across-seep survey lines to achieve three main objectives: (1) to visualize the entire seep, (2) to estimate the seep origin, and (3) to confirm that the across-seep passes were sampling a seep emanating from near the downed jacket.

3. Flow Rate Estimate Methods

The three components necessary for determination of the flow rate are the size, number, and identity of targets. Figure 2 outlines the steps used to determine the total number of gas bubbles and/or oil droplets present, as well as the size of those targets, at each depth in a single across-seep pass. The processing for each across-seep pass was broken down into four steps:

- Step 1: Acoustic mapping of seep position, ADCP measurements of current, and rise velocity models for oil droplets and gas bubbles were used to estimate the size of targets within 0.5-m-depth bins.
- Step 2: All possible combinations of the number of gas bubbles and oil droplets that explained the observed acoustic backscatter in each across-seep pass and 0.5-m-depth bin were identified.
- Step 3: The combination of gas bubbles and oil droplets that best fit the observed frequency-dependence of the acoustic backscatter in each across-seep pass and 0.5-m-depth bin was selected and therefore the identities of the scatterers were determined.
- Step 4: The total volume of gas and oil present in each depth bin was summed to determine the volume of oil and gas in a given across-seep pass.

3.1. Step 1: Size of Targets

Acoustic mapping of the seep was used to determine the depth of the seep as it moved downstream from the origin. The position and depth of the seep was combined with the horizontal current measurements to determine the rise velocity of particles in the seep. Lines of constant rise velocity were projected downstream to determine the rise velocity of particles in each depth bin at each across-seep pass. The depth, z_D of a particle rising with rise velocity, w at distance down stream, D was determined by

$$z_D = \sum_{k=1}^{D} \frac{w(x_k - x_{k-1})}{u(z)}, \tag{1}$$

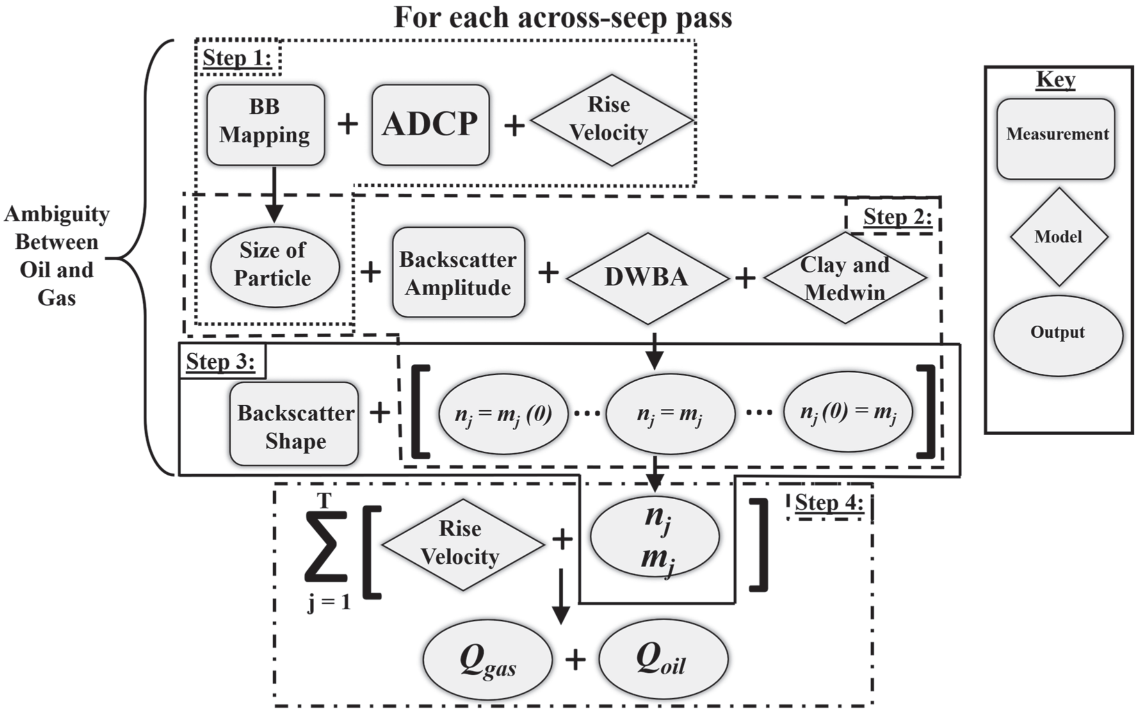

Figure 2. A flow chart of the signal processing methodology used to determine the flow rate, Q, of hydrocarbons in a given across-seep pass. Measurements are combined with models to produce outputs. The output is then combined with another measurement and/or model to produce a new output. Processing occurs independently for each depth bin, j, for Steps 1 to 3 with the following outputs: (1) size of targets, (2) number of targets, and (3) identity of targets (gas and/or oil). In Step 4, the results for all T total depth bins are summed to determine the flow rate of oil and gas in a given across-seep pass. Note that there was an ambiguity between oil and gas until the output of Step 3; n_j and m_j are the number of bubbles and droplets in a depth bin, respectively.

where x_k was the incremental distance downstream and $u(z)$ was the depth-dependent rise velocity. For a given across-seep pass at distance D downstream, each depth bin was associated with a rise velocity.

Oil droplets are assumed to be incompressible with minimal exchange with the surrounding water column and their rise velocities are likely to be constant as they travel downstream. For gas bubbles, however, the size and rise velocity of individual bubbles is affected by both changes in hydrostatic pressure and the exchange of gases with the surrounding water (Dissanayake et al., 2018). This change in rise velocity will cause individual bubbles to cross lines of constant rise velocity as they move down stream. Without knowledge of the chemical composition of gas bubbles or of the aqueous concentration of gases in the water column it was not possible to model the change in bubble size as the bubbles evolve moving downstream. The uncertainty in the evolution of bubbles moving downstream leads to uncertainty in the estimate of the volume of gas using the method described here. Incompressible oil droplets, on the other hand, do not suffer from the same uncertainty in their evolution as they move downstream.

A model of the rise velocity of gas bubbles and oil droplets (Zheng & Yapa, 2000) was then inverted to determine the size of a gas bubble or oil droplet rising with a velocity equal to the local rise velocity. Zheng and Yapa (2000) derived an integrated approach to determining the rise velocity of spherical and nonspherical bubbles and droplets from correlation formulations developed by Clift et al. (1978) for bubbles and droplets in contaminated and pure fluids. It was assumed that the ambient seawater had sufficiently high concentrations of surfactants to be beyond the critical concentration, and the equations for contaminated bubbles were applicable. Zheng and Yapa (2000) found that tap water contained sufficiently high surfactants for the contaminated equations to be a best fit for rising bubbles. Given the highly biologically productive waters in the area surrounding the seep combined with the likelihood of a high sediment load due to the proximity of the site to the mouth of the Mississippi River, it is likely that there were sufficient surfactants to be beyond the critical concentration.

Oil droplets are assumed to be incompressible and their rise velocity not to change with depth. The American Petroleum Institute (API) gravity (a common metric used to define crude oil as either heavy, medium, or light) of oil in the water column at this site was 25.74° consistent with a medium crude oil (Mason et al., 2019). Density and sound speed were modeled according to Loranger et al. (2018). Oil droplets within the ellipsoidal regime (radius < 0.5 mm Clift et al., 1978) were assumed to have an eccentricity of 0.6, the average eccentricity for an oil with similar API gravity reported by Loranger et al. (2019).

The rise velocity of bubbles was modeled using the physical properties of methane as a function of depth. The chemical composition of gas bubbles in the seep as well as the concentration of gases in the water column was unknown. Acoustic backscatter and rise velocity of gas bubbles do not vary significantly between the hydrocarbon gases likely to be present at this site. While composition of the gas in a bubble is unknown, an estimate of the total volume of gases present in the bubble is possible. A separate solution to the rise velocity equations was calculated for each depth by computing the properties of methane as a function of hydrostatic pressure. The bubble size associated with a rise velocity at a given depth was the size of a bubble with properties equal to the properties of methane at hydrostatic pressure. It was noted that rise velocity is primarily a function of bubble radius. For a given bubble size the difference between the rise velocity at 8 m compared with the rise velocity of a bubble of equal size, but with physical properties at the increased pressure at 90 m differed by less than 0.4 mm/s. So while the mass of gas in a bubble at 90-m depth is different than a bubble of equal size at 8 m, the rise velocity is relatively constant.

The output of Step 1 was the radius of bubble or oil droplet associated with each depth bin in each across-seep pass according to the rise velocity of that bin. The radius of the droplet and bubble are not likely to be the same, as smaller gas bubbles rise more quickly than larger oil droplets. Step 1 results in a range of possible sizes for oil droplets and gas bubbles determined by the maximum and minimum rise velocity of the seep. Whether the targets in the bin were oil droplets, gas bubbles, or a combination of the two is described in the subsequent steps.

3.2. Step 2: Number of Targets

To determine the number of targets present in an ensonified volume, backscatter for a range of gas to oil ratios was modeled and the total number of targets for each ratio was iteratively increased until the modeled and measured backscatter reached a minimum root-mean-square (RMS) error.

Weber and Ward (2015) showed that the Fourier transform of the signal recorded by a broadband echosounder, $S_{mf}(f)$, is related to $\sigma_{bs}(f)$, the frequency-dependent backscattering cross-sectional area of a deterministic signal target by

$$\sigma_{bs}(f) = \frac{|S_{mf}(f)|^2}{C_{mf}(f)} \frac{r^4}{e^{-4ar}}, \tag{2}$$

where $C_{mf}(f)$ is the matched filtered correction factor, r is the range to the target in meters, and a is the absorption coefficient in nepers/m. $\sigma_{bs}(f)$ is related to the frequency-dependent target strength (TS(f)) by

$$TS(f) = 10\log_{10}(\sigma_{bs}(f)). \tag{3}$$

When the sample volume is composed of multiple scatterers instead of a discrete scatterer, the target strength becomes, $TS_m(f)$, the target strength of the multiple scatterers combined

$$TS_m(f) = 10\log_{10}(\sigma_T(f)), \tag{4}$$

where $\sigma_T(f)$ is the total summed backscattering cross-sectional areas of all N scatterers in the sample volume assuming that the targets incoherently scatter (Clay & Medwin, 1977; Foote, 1983; Weber et al., 2014) such that

$$\sigma_T(f) = \sum_{i=1}^{N} \sigma_{bs,i}(f). \tag{5}$$

In the case of multiple scatterers the right-hand side of Equation 2 stays the same (it is the calibrated and range-corrected signal recorded by the echosounder) but $\sigma_{bs}(f)$ becomes $\sigma_T(f)$ and

$$\sigma_T(f) = \frac{|S_{mf}(f)|^2}{C_{mf}(f)} \frac{r^4}{e^{-4ar}}. \tag{6}$$

$\sigma_T(f)$, is the backscatter from all sources in the ensonified volume including the backscatter from all targets of interest, $\sigma_t(f)$, as well as the contribution from other targets such as biological scatterers and other sources of noise here defined as $\sigma_{bg}(f)$, the contribution to scattering from background targets (De Robertis & Higginbottom, 2007). Therefore $\sigma_T(f)$ is

$$\sigma_T(f) = \sigma_t(f) + \sigma_{bg}(f). \tag{7}$$

Combining Equations 6 and 7 the scattering from the targets of interest $\sigma_t(f)$ becomes,

$$\sigma_t(f) = \frac{|S_{mf}(f)|^2}{C_{mf}(f)} \frac{r^4}{e^{-4ar}} - \sigma_{bg}(f). \tag{8}$$

If $\sigma_t(f)$ has a bimodal distribution such as a scattering volume composed of oil droplets and gas bubbles, then $\sigma_t(f)$ can be approximated as

$$\sigma_t(f) \approx n\overline{\sigma}_{bs,n}(f) + m\overline{\sigma}_{bs,m}(f), \tag{9}$$

where $\overline{\sigma}_{bs,n}(f)$ is the average backscattering cross sectional area of the n targets of the first mode of the distribution, and $\overline{\sigma}_{bs,m}(f)$ is the average backscattering cross-sectional area of the m targets of the second mode. Combining Equations 8 and 9 results in

$$n\overline{\sigma}_{bs,n}(f) + m\overline{\sigma}_{bs,m}(f) = \frac{|S_{mf}(f)|^2}{C_{mf}(f)} \frac{r^4}{e^{-4ar}} - \sigma_{bg}(f). \tag{10}$$

Equation 10 compares the modeled backscatter (left-hand side, LHS) to the measured backscatter (right-hand side, RHS) with two scaling factors n and m. The measured backscatter was determined by summing the raw wave forms from the four quadrants of the broadband split beam echosounder. The summed wave forms were then matched filtered using an idealized transmit pulse. The resulting matched filtered signal was binned into 0.5-m-depth bins with no overlap. The Fourier transform of the 0.5-m-depth bins was then taken to determine $S_{mf}(f)$. Each depth bin encompassed 63 samples, resulting in a frequency spacing of about 1.5 kHz.

The split-beam echosounder used in this experiment measures the angle of a target within the acoustic beam. The intensity as a function of frequency in a depth bin was then averaged across all pings where the seep was within 3° of the center of the beam to determine the average backscatter as a function of frequency $\hat{S_{mf}}(f, z)$. According to the beam angle information the target was constrained within the beam and therefore the intensity, and not the intensity per unit volume, was averaged across pings (see supporting information). $\hat{S_{mf}}(f, z)$ was then used to determine the first term on the right-hand side (RHS) of Equation 10 with the absorption coefficient, a, for each frequency determined by the model by Francois and Garrison (1982).

The second term on the RHS of Equation 6, $\sigma_{bg}(f)$, was determined using a method similar to that described by De Robertis and Higginbottom (2007). The same summing, matched filtering, Fourier transform, and averaging methodology was used as described above for $\hat{S_{mf}}(f, z)$ on 100 pings adjacent to the seep—where no seep was evident in the water column. Equation 6 was then applied to to the resulting background signal $\hat{S_{bg}}(f, z)$ to determine $\sigma_{bg}(f)$. The difference between the two terms on the RHS of Equation 10 was then smoothed using a moving average filter.

To model the backscatter in the seep at MC20, it was assumed that individual targets were either gas bubbles or oil droplets. This method neglects the contribution to the oil budget from oil coated gas bubbles, such as those detected at this site by Mason et al. (2019). It also assumes that the oil coating on a gas bubble will not impact the backscatter and that the bubble can be modeled as a pure gas bubble. Coatings on gas bubbles are frequently ignored in acoustic scattering modeling as the scattering from the thin coating is negligible when compared with the scattering from the bubble (e.g., Weber et al., 2014). Neglecting the contribution to the oil budget from oil-coated bubbles could cause the results of this study to underestimate the total oil flow rate if oil coatings on gas bubbles are a significant source of oil.

The backscatter for individual gas bubbles, $\overline{\sigma}_{bs,n}(f)$, was modeled according to Clay and Medwin (1977) with a correction by Ainslie and Leighton (2009), while the backscatter for individual oil droplets, $\overline{\sigma}_{bs,m}(f)$, was modeled using the distorted wave Born approximation (Loranger et al., 2019; Stanton et al., 1998). The radius

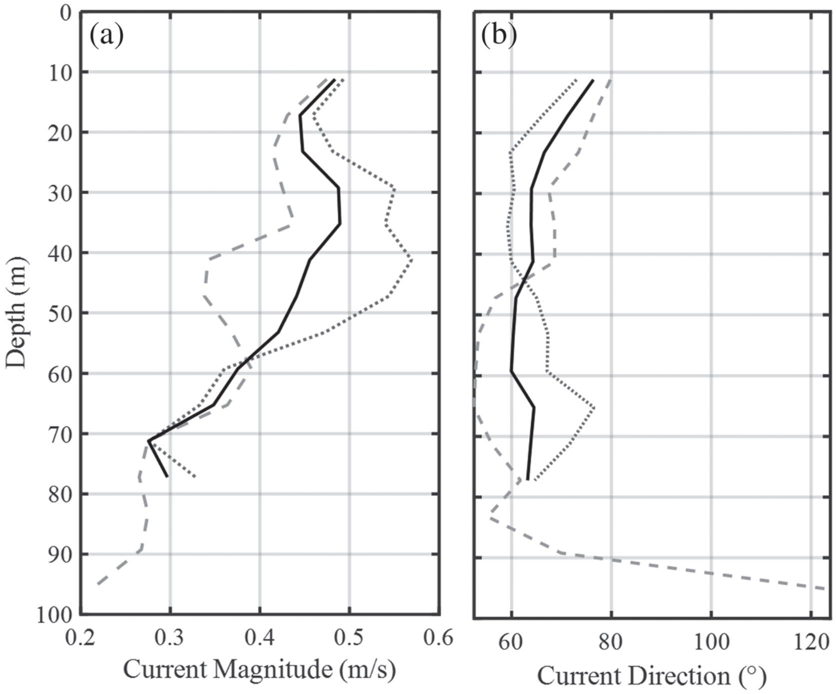

Figure 3. ADCP survey results. (a) The magnitude and (b) the direction of the current for the first ADCP survey (gray dashed line) and second ADCP survey (gray dotted line). The two surveys were averaged together to estimate the current over the WBT survey period (black sold line) for depths less than 77.2 m. For greater depths measurements from the first survey measurements were used.

of bubbles a_j and droplets b_j from Step 1 was used to calculate $\overline{\sigma}_{bs,n}(f)$ and $\overline{\sigma}_{bs,m}(f)$ in 0.5-m-depth bins. This assumes that all the particles in a 0.5-m-depth bin are represented by the radius of the particle in the center of the bin. This discretization of the particle size distribution has minimal impact on the calculation of flow rate. With 0.5-m bin spacing, the average difference between particle sizes in adjacent bins was 16 microns.

The total number of targets was then be determined by iteratively increasing n and m until the RMS error between the LHS and RHS of Equation 10 reaches a minimum. n and m were determined for ratios of n:m ranging from 1:0 to 0:1 in increments of 0.01. The output of Step 2 was 101 different values of n and m, one value for each potential ratio of n:m.

3.3. Step 3: Identity of Targets

To determine which ratio of n:m best fits the measured backscatter, the RMS errors from each of the 101 ratios of n:m were compared. Each of the RMS errors provides a measure of how well each combination of n and m fits the measured backscatter frequency response. The ratio of n:m that results in the smallest RMS error between the LHS and RHS of Equation 10 was determined to be the estimate of the ratio of oil to gas at a given depth and across-seep pass. The output of Step 3 is the best fit n and m that, in combination, provided the best match to the measured backscatter.

3.4. Step 4: Total Flow Rate

The total flow rate of oil and gas in an individual across-seep pass was then determined by summing the flow rates of oil and gas independently in each depth bin, j, according to

$$\begin{aligned} Q_{oil} &= \sum_{j=1}^{T}\left[\frac{4\pi(a_j)^3(n_j)(w_j)}{3(\Delta z)}\right] \\ Q_{gas} &= \sum_{j=1}^{T}\left[\frac{4\pi(b_j)^3(m_j)(w_j)}{3(\Delta z)}\right], \end{aligned} \tag{11}$$

where T was the total number of depth bins in across-seep pass j, a_j, and b_j were the radius of a bubble and droplet, respectively, at depth j in Step 1. The n_j and m_j were the number of bubbles and droplets, respectively,

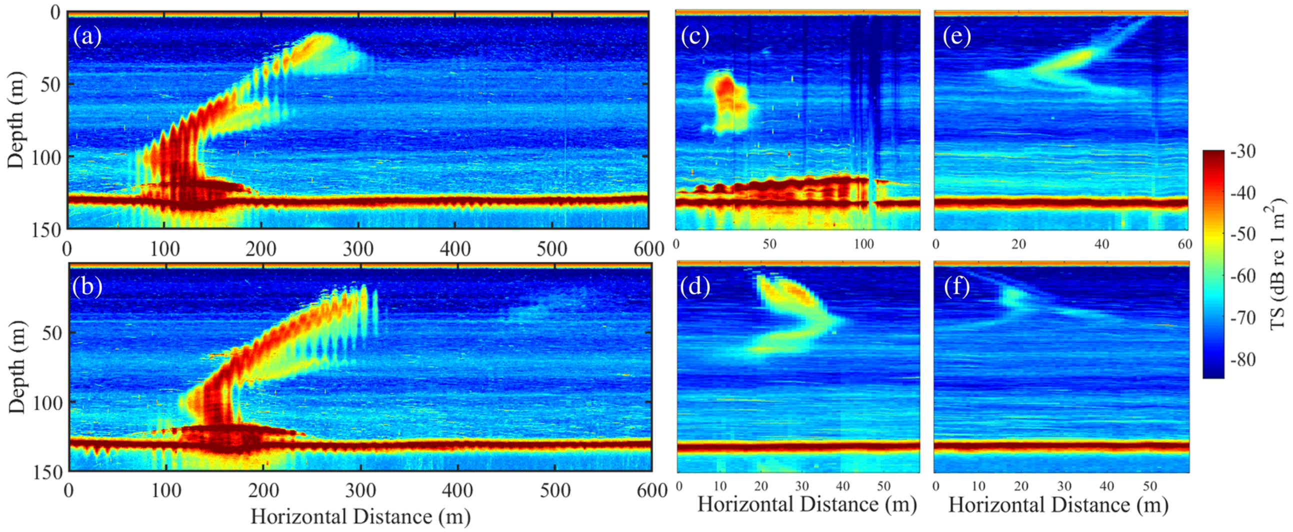

Figure 4. Broadband acoustic echograms for along seep (a and b) and across seep (c–f) passes. Panels (a) and (b) show examples of two of nine lines that run parallel to the nominal direction of flow. Motion artifacts can be seen in the along-seep survey lines due to increased sea state during these survey lines. The downed jacket is visible on the seafloor as a high TS return parallel to the seafloor at about 125 m. Panels (c–f)show echograms for cross-sectional passes at increasing distance downstream of the seep origin. Panel (c) is the echogram closest to the origin (58 m), followed by (d) (115 m), then (e) (187 m), and (f) (235 m).

from Step 2 that best fit the shape of the broadband backscatter as determined in Step 3. w_j was the rise velocity at depth j and Δz was the width of the depth bin.

4. Survey Results

Two ADCP surveys were performed, one before and one after the echosounder surveys (Table 2). Sea state rose considerably by the time of the second ADCP survey, and the increased sea state resulted in a shallower second ADCP survey. The last good depth (the deepest depth with data that pass the exclusion criteria) for the first survey was 95.2 m, and the last good depth for the second ADCP survey was 77.2 m. For depths where there were measurements from both surveys (8.2 to 77.2 m), the two showed close agreement in both magnitude and direction as function of depth and they were averaged together (Figure 3). The surveys revealed a current to the east-northeast that decreased in magnitude with depth to a depth of 90 m. Below 90 m a deep water, low-magnitude current 90° offset from the shallower current was found heading to the east-southeast. The flow rate estimate method in this study was dependent on measurements from the ADCP to determine the rise velocity. While the downed jacket rests on the seafloor at about 135-m depth, the analysis of the flow rate in this study was limited to depths where ADCP data was present, from 95.2 to 8.2 m.

Thirteen total across-seep echosounder survey lines were run in which the seep was present. Two lines that run downstream of the source detected no seep and lines that run greater than 350 m upstream also detected no seep. The shallowest part of the seep reached the surface at about 115 m downstream of the source. The entire seep was within the range of the ADCP measurements by 38 m downstream from the origin. Figures 4c–4f show example echograms from 4 of the 13 passes.

Nine along-seep surveys were performed where the seep was present in the echogram. The along-seep echograms show a seep where the fastest rise velocity targets at the top of the seep have a strong target strength compared to the lower rise velocity targets (Figures 4a and 4b). This causes the appearance of a high backscattering "spine" of targets at the top of the seep, and a lower backscattering section below the seep. Note that the narrowness of the seep and the increased seas during the along-seep passes resulted in the seep coming into and out of the acoustic beam during individual along-seep lines, for example, in Figure 4a the seep moves out of the beam at around 200 m horizontal distance. However, for lines where the seep moved out of the beam, the seep was detected at the gaps in one line by at least one other along-seep line. The increased sea state also resulted in the presence of motion artifacts in the along-seep survey lines. These artifacts are not evident in the across-seep passes used to determine the flow rate. The counter current at depths below 100 m coincides with where the seep bends to the left in the echograms (in the upstream direction) before the seep continues to move downstream for shallower depths.

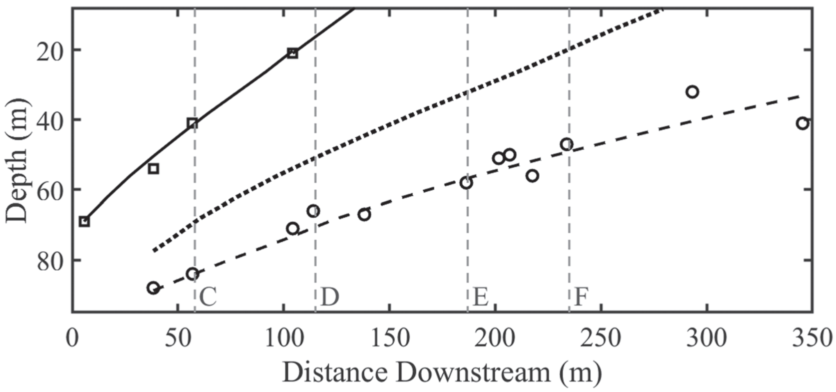

Figure 5. Lines of constant rise velocity project downstream. Black boxes show the location of the shallowest part of the seep as determined visually from echo grams, while black circles show the deepest part of the seep. Three example lines of constant rise velocity are shown, 21.3 cm/s (solid), 11.3 cm/s (dotted), and 6.7 cm/s (dashed). The location of the echograms in Figures 4c–4f are shown as vertical gray lines.

5. Signal Processing Results

5.1. Step 1: Size of Targets

Lines of constant rise velocity were determined starting from the first across-seep pass where the entire seep was within the ADCP measurement range, 38 m downstream from the origin (Figure 5). The shallowest part of the seep fit with a constant rise velocity of 21.3 cm/s ($r^2 = 0.99$, $p = 0.004$) while the deepest part of the seep fit with a rise velocity of 6.7 cm/s ($r^2 = 0.91$, $p < 0.001$).

The rise velocity for oil droplets, according to the model by Zheng and Yapa (2000), reaches a maximum of 11.3 cm/s for 3.0 mm radius droplets (Figure 6). For droplets larger than 3.0 mm, the rise velocity reaches a plateau. It was conservatively assumed that for any rise velocity where there was an ambiguity in the size of an oil droplet, the droplet was the smallest size possible. Therefore, all droplets at the maximum rise velocity of 11.3 cm/s were 3.0 mm in radius, and no droplets larger than 3.0 mm were present in the seep. This assumption could lead to an underestimate of the total flow rate of oil if droplets larger than 3.0 mm were present. The minimum rise velocity in the seep, 6.7 cm/s, coincides with droplets with radius 1.2 mm. Droplets in the seep varied in radius from 1.2 to 3.0 mm.

Any part of the seep with a rise velocity greater than 11.3 cm/s was assumed to contain only bubbles, as droplets are predicted to rise with a maximum velocity of 11.3 cm/s. The value 11.3 cm/s was the rise velocity for a bubble of radius 0.49 mm. The bubble radius for the maximum rise velocity of the seep, 21.3 cm/s,

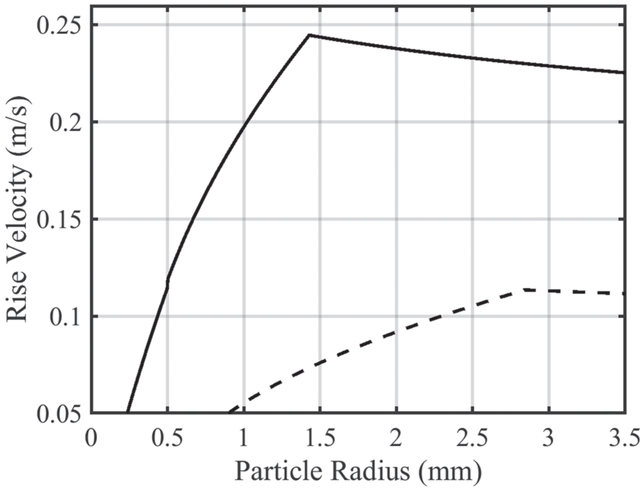

Figure 6. The rise velocity and particle radius for oil droplets (dashed line) and methane bubbles (solid line) as modeled according to Zheng and Yapa (2000).

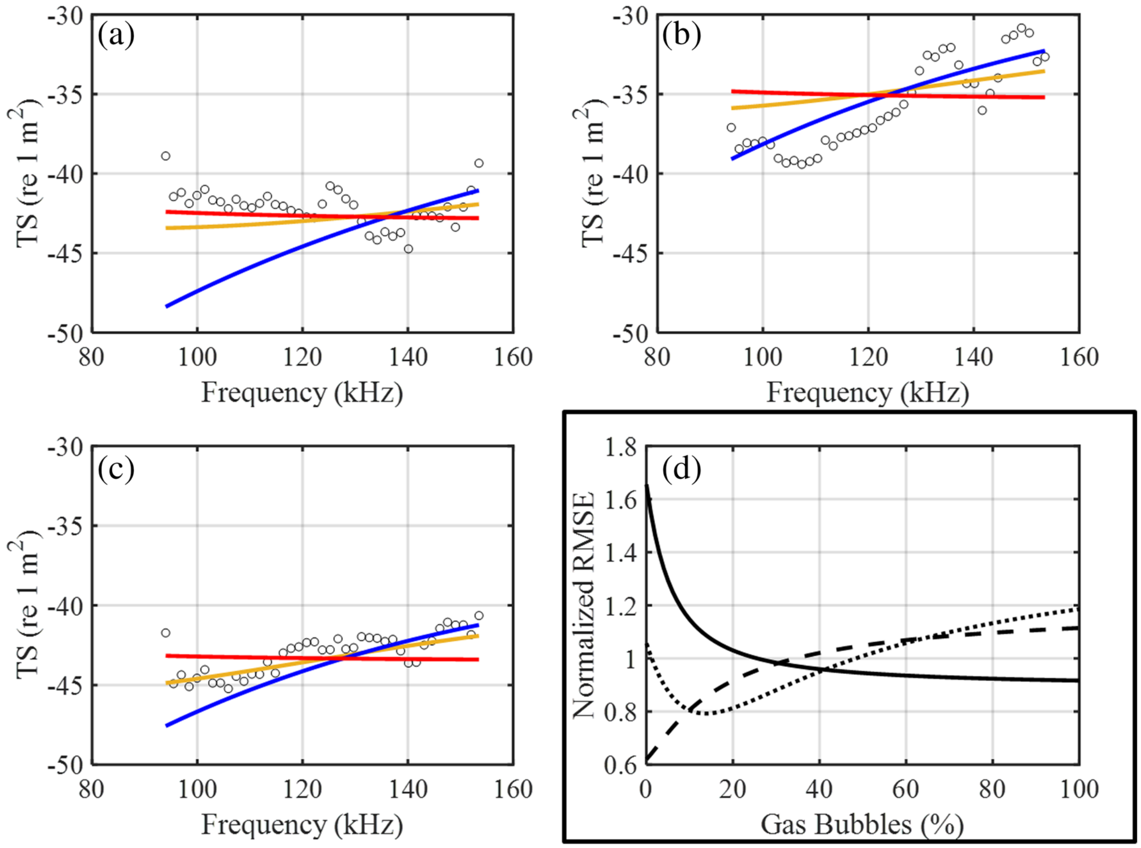

Figure 7. The measured frequency-dependent target strength (10 $\log_{10}(\sigma_t)$, black circles) for three different depths (a = 55 m, b = 65 m, c = 45 m) and distances down stream (a = 187 m, b = 115 m, c = 203 m). The red line in a, b, and c shows the modeled backscatter case where all targets are gas bubbles, the blue line is the case where all targets are oil droplets, and the orange line shows the case where there is a mixture of targets (14% gas bubbles and 86% oil droplets). Figure 7d shows the normalized RMS error between the modeled and measured backscatter for each of the ratios of n:m modeled in Step 2 for (a) (solid line), (b) (dashed line), and (c) (dotted line).

corresponded to a 1.2 mm bubble while the slowest rise velocity of the seep, 6.3 cm/s, corresponded to a 0.29 mm bubble. It was assumed, therefore, that bubbles ranged in size from 0.29 to 1.2 mm. Within the region of the seep predicted to contain oil droplets (sections with rise velocities equal to or less than 11.3 cm/s) bubbles ranged from 0.29 to 0.49 mm.

In a given across-seep pass the rise velocity, and therefore the particle radius, was determined in 0.5-m-depth bins. It was assumed that in each depth bin, the droplets and bubbles were each of a different, but singular size. So in the depth bin associated with the slowest rise rate, 6.3 cm/s, any droplets in that depth bin were 1.2 mm, while any bubbles present would be 0.29 mm in radius. This assumption results in a discrete particle size distribution in each pass. The droplet size distribution in each pass ranged from 1.2 to 3.0 mm with an average spacing of 18 μm. The bubble size distribution ranged from 0.49 to 1.2 mm with an average spacing of 14 μm. The smaller bubble sizes and droplet sizes were present in each pass while larger droplets (dashed line in Figure 5) reached the surface at a downstream distance of ~275 m and the larger bubbles reached the surface at downstream distance of ~125 m.

5.2. Step 2: Number of Targets

Figures 7a–7c shows three examples comparing the modeled backscatter (LHS of Equation 10) and measured backscatter (RHS of Equation 10) for three ratios of n:m. For the modeled case where all targets are bubbles, the frequency response was flat, where as for the case where all targets were droplets, the frequency response increased in amplitude with increasing frequency. For mixtures of gas and oil, the modeled frequency response was between the all gas bubble case and the all oil droplet case, with a slope that decreased with increasing ratio of n:m. For cases where the seep had split into two sections in the echogram (such as the deeper portions of Figures 4e and 4f and the upper part of Figure 4d), n and m were calculated for each section separately and then summed as a function of depth.

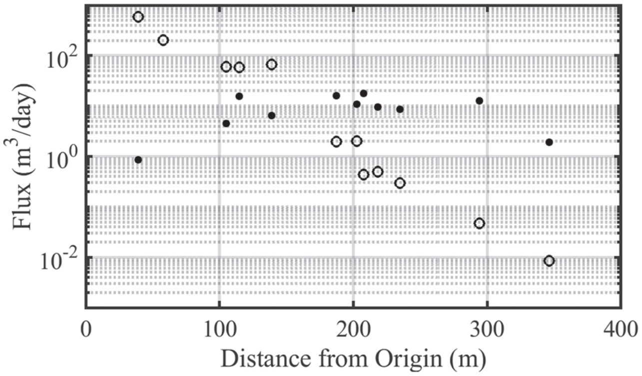

Figure 8. The depth-integrated flow rate (m^3/day) of oil (solid black circles) and gas (open black circles) for each cross section of the seep by distance from the seep origin. Note that for the pass at 58 m from the origin, there was no oil detected.

5.3. Step 3: Identity of Targets

Figure 7d shows the range of RMS errors for the 101 ratios of n:m for each of the three examples in a, b, and c. Step 2 produced 101 RMS errors, one for each ratio of n:m. The best fit, and therefore the identity of the scatterers at a given depth and across-seep pass was the ratio of n:m with the smallest RMS error. The RMS errors in Figure 7d are normalized for comparison by the average RMS error for all ratios of n:m at a given depth and pass. The minimum RMS error for Figure 7a corresponds to the red line, the case where all targets are bubbles ($n = 502$, $m = 0$). For Figure 7b the minimum RMS error corresponds to the blue line, where all targets are droplets (N = 0, M = 21,031). For Figure 7c the minimum RMS error corresponds to the orange line, a mixture of gas and oil (N = 147, M = 902).

The oil-gas ratio that best fit the observations was, on average, 88% of the average RMS error at that depth and across-seep pass. On average the RMS error of the best fit model was 12% smaller than the average RMS error at a given depth and across-seep pass. The maximum RMS error, or the RMS error of the worst fit oil-gas ratio, was 130% of the average RMS error. For the examples in Figure 7, the minimum RMS error was 92%, 62%, and 79% of the average RMS error for Figures 7a–7c, respectively.

For cases where the seep had split into two sections (see supporting information), the ratio with the minimum RMS error was calculated separately for each section and then n and m from each seep were combined to get the total targets at that depth. Therefore, at a given depth and across-seep pass where this seep had split, it was possible to have two different ratios of n:m, one for each section of the seep.

5.4. Step 4: Flow Rate of Oil and Gas

The size, a_j and b_j, and number, n_j and m_j, of bubbles and droplets respectively determined in Steps 1–3 for each depth, j, was used to determine the total flow rate, Q, for each across-seep pass according to Equation 11 (Figure 8). For the first two passes over the seep almost no oil was detected. This was likely due to the relatively short time period between release of oil and gas from the seafloor source and transport to the two passes that were less than 60 m downstream. The oil and gas had not had sufficient time to separate vertically in the water column, and the stronger scattering from gas likely masked the oil in these passes. The fastest rising oil droplets reach the surface at a downstream distance of about 280 m, meaning that some of the oil has reached the surface by the final across-seep pass. The two passes closest to the origin and the pass at the greatest distance downstream were excluded from the total average flow rate calculation. The average total flow rate of oil was 71 barrels/day. (Including all passes the average flow rate was 54 barrels/day). The 95% confidence interval for the total flow rate of oil was 56 to 86 barrels/day assuming that the sample standard deviation over the nine passes is an accurate estimation of the true standard deviation (Bendat & Piersol, 2000). The flow rate of oil does not change as the oil moves downstream, consistent with the assumption that dissolution of oil into the water column is negligible.

The fastest rising gas bubbles will reach the surface at just over 130 m downstream. Calculation of the total gas flow rate was limited to the four passes closest to the origin, before the gas reached the surface. The total gas flow rate was 229 m^3/day with a range of 98 to 359 m^3/day (Figure 8). The volume of gas was for gas corrected to standard surface temperature and pressure. The flow rate of gas decreases as the gas moves downstream of the source, due to gas dissolving into the surrounding water column, and gas reaching the sea surface and entering the atmosphere.

6. Discussion and Conclusions

The estimate of total flow rate of liquid hydrocarbons from the shipboard surveys in this study, 56 to 86 barrels/day, was within the estimates from surface methods (48 to 1,700 barrels/day Sun et al., 2018), and from visual ROV methods (19 to 108 barrels/day Mason et al., 2019), with a narrower range (Table 1). The flow rate of oil estimated in this study was higher than hybrid shipboard and ROV methods (9 to 47 barrels/day) and slightly more narrow in range. This study also found a flow rate higher than the containment system estimate of 24 to 31 barrels/day. This study neglects the contribution of oil-coated gas bubbles to the total oil flow rate and assumes that no droplets greater than 3.0 mm radius were present, therefore the estimate of oil flow rate was potentially underestimated.

The containment system estimate was made from a single measurement, the collection of oil by the system over 30 days. The other flow rate estimates made at MC20 were made from multiple measurements made over different time scales, and at different times. The width of the range of flow rate estimates increases with increasing time scale of the measurement (Table 1). The difference in the width and value of the flow rate estimate could be due to either different biases inherent in the different methodologies, or to variation in the flow rate over time. Previous studies from natural seeps have found that flow rate can vary on the scale of hours and on tidal cycles (Boles et al., 2001; Jerram et al., 2015). This variability could explain the difference between the estimates made over different time scales and in different years at this site. Finer temporal scale measurements of the flow rate of liquid hydrocarbons from seafloor sources are required to determine how the flow rate varies over increasing time scales (hours, tidal cycles, seasons, years, etc.) and to determine how to interpret the differences in flow rate between methods.

The flow rate of liquid hydrocarbons at MC20 from this study varied in value and range from estimates made over different time scales using different methodologies (Table 1). Whether this was due to biases in the methodologies or variability in the flow rate from this source over time is unknown. For example, to compare the shipboard method used in this study to the direct containment system flow rate, a longer shipboard survey period that encompasses different forcing regimes, (e.g., tides, changes to horizontal currents, changes in outflow from the Mississippi River) over a time scale similar to the containment system would be necessary to determine if the difference between the total flow rate estimates was due to the longer time average of the containment system or to some bias in the acoustic measurements. Alternatively, finer temporal resolution measurements of flow rate from the containment system could elucidate the temporal variability of the seep and indicate if the shipboard survey estimates are within the range of flow rate values for the shorter time scale of the surveys. To better understand how to interpret flow rate estimates from seafloor hydrocarbon sources, and to understand the proper time scale over which measurements should be made, it is necessary to measure the flow rate at finer time scales over longer periods than currently available.

A further aid to classification of oil droplets and gas bubbles would be the addition of broader frequency range, especially lower frequencies, to the echosounders used in surveying the site. With a broader range of frequencies it may be possible to detect the peak and null structure of individual droplets which would aid in determining the size as well as the identity of oil droplets (Loranger et al., 2019). At low frequencies, the difference between the target strength of oil droplets and gas bubbles is much more pronounced. Gas bubbles exhibit resonance scattering where the wavelength is larger than the radius of the bubble and oil droplets do now (Weber et al., 2012). Gas bubbles are easily detected at the low frequencies where the wavelength is larger, while oil droplets are unlikely to be detected. The presence/absence of targets in the low frequencies would provide further evidence of the identity of scatterers.

The shipboard broadband acoustic survey methodology was capable of determining the flow rate of hydrocarbons and to constrain the flow rate to a more narrow range than the visual ROV survey and the hybrid shipboard and ROV methods. The diverse range of methods used at MC20 resulted in an equally diverse estimate of the flow rate. The differences among flow rate estimates is potentially due to changes in the flow rate of the seep. Determination of what processes drive changes to the flow rate from seafloor seeps is critical to understanding how to interpret flow rate estimates, and how to use those estimates to determine natural flow of hydrocarbons from natural seeps and to predict the impact of seafloor sourced anthropogenic spills on the marine environment.

Data Availability Statement

Survey data are available at the NOAA National Center for Environmental Information repository (https://doi.org/10.25921/910v-v249).

Acknowledgments
We thank the crew of the Gerry Bordelon and T. J. Broussard of the Bureau of Safety and Environmental Enforcement. The work was supported by the National Oceanic and Atmospheric Administration (Grant NA15NOS4000200).

References

Ainslie, M. A., & Leighton, T. G. (2009). Near resonant bubble acoustic cross-section corrections, including examples from oceanography, volcanology, and biomedical ultrasound. *The Journal of the Acoustical Society of America*, *126*, 2163–2175. https://doi.org/10.1121/1.3180130

Bendat, J. S., & Piersol, A. G. (2000). *Random data: Analysis and measurement procedures*. New York, NY: Wiley. https://doi.org/10.2307/2981634

Boles, J. R., Clark, J. F., Leifer, I., & Washburn, L. (2001). Temporal variation in natural methane seep rate due to tides, Coal Oil Point area, California. *Journal of Geophysical Research*, *106*(C11), 27,077–27,086. https://doi.org/10.1029/2000JC000774

Camilli, R., Di Iorio, D., Bowen, A., Reddy, C. M., Techet, A. H., Yoerger, D. R., et al. (2012). Acoustic measurement of the Deepwater Horizon Macondo well flow rate. *Proceedings of the National Academy of Sciences of the United States of America*, *109*(50), 20,235–20,239. https://doi.org/10.1073/pnas.1100385108

Clay, C. S., & Medwin, H. (1977). *Acoustical oceanography: Principles and applications*. New York: John Wiley & Sons. https://doi.org/10.1017/S0025315400028228

Clift, R., Grace, J. R., & Weber, M. E. (1978). *Bubbles, drops, and particles*. New York, NY: Academic Press.

Daneshgar Asl, S., Amos, J., Woods, P., Garcia-Pineda, O., & MacDonald, I. R. (2016). Chronic, anthropogenic hydrocarbon discharges in the Gulf of Mexico. *Deep Sea Research Part II: Topical Studies in Oceanography*, *129*, 187–195. https://doi.org/10.1016/J.DSR2.2014.12.006

De Robertis, A., & Higginbottom, I. (2007). A post-processing technique to estimate the signal-to-noise ratio and remove echosounder background noise. *ICES Journal of Marine Science*, *64*(6), 1282–1291. https://doi.org/10.1093/icesjms/fsm112

Demer, D. A., Berger, L., Bernasconi, M., Bethke, E., Boswell, K., Chu, D., et al. (2015). Calibration of acoustic instruments. *ICES Cooperative Research Report (326)*.

Dissanayake, A. L., Gros, J., & Socolofsky, S. A. (2018). Integral models for bubble, droplet, and multiphase plume dynamics in stratification and crossflow. *Environmental Fluid Mechanics*, *18*(5), 1167–1202. https://doi.org/10.1007/s10652-018-9591-y

Fingas, M., & Brown, C. E. (2018). A review of oil spill remote sensing. *Sensors*, *18*(1), 91. https://doi.org/10.3390/s18010091

Foote, K. G. (1983). Linearity of fisheries acoustics, with addition theorems. *Journal of the Acoustical Society of America*, *73*(6), 1932–1940. https://doi.org/10.1121/1.389583

Francois, R. E., & Garrison, G. R. (1982). Sound absorption based on ocean measurements. Part II: Boric acid contribution and equation for total absorption. *The Journal of the Acoustical Society of America*, *72*(6), 1879–1890. https://doi.org/10.1121/1.388673

Harrison, S. J. (2017). Lessons from the Taylor Energy oil spill: History, seasonality, and nutrient limitation (Unpublished doctoral dissertation), University of Georgia.

Herbst, L., DeCola, E., & Kennedy, K. (2016). New pathways for developing and testing oil spill response equipment in real world conditions. *OCEANS 2016 MTS/IEEE Monterey* (pp. 1–6). Monterey, CA: IEEE. https://doi.org/10.1109/OCEANS.2016.7761477

Holliday, D. V. (1972). Resonance structure in echoes from schooled pelagic fish. *The Journal of the Acoustical Society of America*, *51*(4B), 1322–1332. https://doi.org/10.1121/1.1912978

Hornafius, J. S., Quigley, D., & Luyendyk, B. P. (1999). The world's most spectacular marine hydrocarbons seeps (Coal Oil Point, Santa Barbara Channel, California): Quantifications of emissions. *Jounral of Geophysical Research*, *104*(C9), 20,703–20,711.

Hu, C., Feng, L., Holmes, J., Swayze, G. A., Leifer, I., Melton, C., et al. (2018). Remote sensing estimation of surface oil volume during the 2010 Deepwater Horizon oil blowout in the Gulf of Mexico: Scaling up AVIRIS observations with MODIS measurements. *Journal of Applied Remote Sensing*, *12*(02), 1. https://doi.org/10.1117/1.JRS.12.026008

Jerram, K., Weber, T. C., & Beaudoin, J. (2015). Split-beam echo sounder observations of natural methane see variability in the northern Gulf of Mexico. *Geochemistry, Geophysics, Geosystems*, *15*, 736–750. https://doi.org/10.1002/2014GC005429

Lavery, A. C., Chu, D., & Moum, J. N. (2010). Measurements of acoustic scattering from zooplankton and oceanic microstructure using a broadband echosounder. *ICES Journal of Marine Science*, *67*(2), 379–394. https://doi.org/10.1093/icesjms/fsp242

Loranger, S., Bassett, C., Cole, J. P., Boyle, B., & Weber, T. C. (2018). Acoustically relevant properties of four crude oils at oceanographic temperatures and pressures. *The Journal of the Acoustical Society of America*, *144*(5), 2926–2936. https://doi.org/10.1121/1.5078606

Loranger, S., Pedersen, G., & Weber, T. C. (2019). Broadband acoustic scattering from oblate hydrocarbon droplets. *The Journal of the Acoustical Society of America*, *146*(2), 1176–1188. https://doi.org/10.1121/1.5121699

MacDonald, I. R., Garcia-Pineda, O., Beet, A., Daneshgar Asl, S., Feng, L., Graettinger, G., et al. (2015). Natural and unnatural oil slicks in the Gulf of Mexico. *Journal of Geophysical Research: Oceans*, *120*, 8364–8380. https://doi.org/10.1002/2015JC011062

Mason, A. L., Taylor, J. C., & Macdonald, I. R. (2019). An integrated assessment of oil and gas release into the marine environment at the former Taylor Energy MC20 site. *NOAA Technical Memorandum NOS NCCOS*, *260*, 147. https://doi.org/10.25923/kykm-sn39

Medwin, H., & Breitz, N. D. (1989). Ambient and transient bubble spectral densities in quiescent seas and under spilling breakers. *Journal of Geophysical Research*, *94*(C9), 12,751–12,759. https://doi.org/10.1029/JC094iC09p12751

Padilla, A. M., Loranger, S., Kinnaman, F. S., Valentine, D. L., & Weber, T. C. (2019). Modern assessment of natural hydrocarbon gas flux at the Coal Oil Point seep field, Santa Barbara, California. *Journal of Geophysical Research: Oceans*, *124*, 2472–2484. https://doi.org/10.1029/2018JC014573

Stanton, T. K., & Chu, D. (2008). Calibration of broadband active acoustic systems using a single standard spherical target. *The Journal of the Acoustical Society of America*, *124*(1), 128–136. https://doi.org/10.1121/1.2917387

Stanton, T. K., Chu, D., Jech, J. M., & Irish, J. D. (2010). New broadband methods for resonance classification and high-resolution imagery of fish with swimbladders using a modified commercial broadband echosounder. *ICES Journal of Marine Science*, *67*(2), 365–378. https://doi.org/10.1093/icesjms/fsp262

Stanton, T. K., Chu, D., & Wiebe, P. H. (1998). Sound scattering by several zooplankton groups. II. Scattering models. *The Journal of the Acoustical Society of America*, *103*(1), 236. https://doi.org/10.1121/1.421110

Staves, J., Robinson, L., & Aurand, D. (2013). Ecological risk assessment: Consensus workshop. An examination of the potential ecological impacts of response alternatives being considered for sheen abatement for the remnants of the Taylor Energy Company, LLC MC-20A Platform - Gulf of Mexico. (Tech. Rep.)

Sun, S., Hu, C., Garcia-Pineda, O., Kourafalou, V., Le Hénaff, M., & Androulidakis, Y. (2018). Remote sensing assessment of oil spills near a damaged platform in the Gulf of Mexico. *Marine Pollution Bulletin*, *136*, 141–151. https://doi.org/10.1016/J.MARPOLBUL.2018.09.004

Terrill, E. J., & Melville, W. K. (2000). A broadband acoustic technique for measuring bubble size distributions: Laboratory and shallow water measurements. *Journal of Atmospheric and Oceanic Technology*, *17*(2), 220–239. https://doi.org/10.1175/1520-0426(2000)017<0220:ABATFM>2.0.CO;2

Thompson, C. H., & Love, R. H. (1996). Determination of fish size distributions and areal densities using broadband low-frequency measurements. *ICES Journal of Marine Science*, *53*(2), 197–201. https://doi.org/10.1006/jmsc.1996.0022

Turin, G. L. (1960). An introduction to matched filters. *IRE Transactions of Information Theory*, *IT-6*, 311–329.

Vagle, S., & Farmer, D. M. (1992). The measurement of bubble-size distributions by acoustical backscatter. *Journal of Atmospheric and Oceanic Technology*, *9*(5), 630–644. https://doi.org/10.1175/1520-0426(1992)009<0630:TMOBSD>2.0.CO;2

Warren, C. J., MacFadyen, A., & Henry, C. (2014). Mapping oil for the destroyed Taylor Energy site in the Gulf of Mexico. *International Oil Spill Conference Proceedings*, *2014*(1), 299931. https://doi.org/10.7901/2169-3358-2014-1-299931.1

Weber, T. C., De Robertis, A., Greenaway, S. F., Smith, S., Mayer, L., & Rice, G. (2012). Estimating oil concentration and flow rate with calibrated vessel-mounted acoustic echo sounders. *Proceedings of the National Academy of Sciences of the United States of America*, *109*(50), 20,240–20,245. https://doi.org/10.1073/pnas.1108771108

Weber, T. C., Mayer, L., Jerram, K., Beaudoin, J., Rzhanov, Y., & Lovalvo, D. (2014). Acoustic estimates of methane gas flux from the seabed in a 6000 km^2 region in the Northern Gulf of Mexico. *Geochemistry, Geophysics, Geosystems*, *15*, 1911–1925. https://doi.org/10.1002/2014GC005271

Weber, T. C., & Ward, L. G. (2015). Observations of backscatter from sand and gravel seafloors between 170 and 250 kHz. *The Journal of the Acoustical Society of America*, *138*(4), 2169–2180. https://doi.org/10.1121/1.4930185

Weidner, E., Weber, T. C., Mayer, L., Jakobsson, M., Chernykh, D., & Semiletov, I. (2019). A wideband acoustic method for direct assessment of bubble-mediated methane flux. *Continental Shelf Research*, *173*, 104–115. https://doi.org/10.1016/j.csr.2018.12.005

Wiggins, S. M., Leifer, I., Linke, P., & Hildebrand, J. A. (2015). Long-term acoustic monitoring at North Sea well site 22/4b. *Marine and Petroleum Geology*, *68*, 776–788. https://doi.org/10.1016/j.marpetgeo.2015.02.011

Zheng, L., & Yapa, P. D. (2000). Buoyant velocity of spherical and nonspherical bubbles/droplets. *Journal of Hydraulic Engineering*, *126*(11), 852–854. https://doi.org/10.1061/(ASCE)0733-9429(2000)126:11(852)